# Simulational validation of color magnetic particle imaging (cMPI)



2014 Phys. Med. Biol. 59 6521

(http://iopscience.iop.org/0031-9155/59/21/6521)

IOP Publishing | Institute of Physics and Engineering in Medicine Physics in Medicine & Biology

Phys. Med. Biol. **59** (2014) 6521–6536 doi:10.1088/0031-9155/59/21/6521

# Simulational validation of color magnetic particle imaging (cMPI)

**S H Han[1], E Cho[1], D K Lee[1], G Cho[2], Y R Kim[1,3] and H Cho[1]**

[1] Ulsan National Institute of Science and Technology, Ulsan, Korea
[2] Korea Basic Science Institute, Ochang, Korea
[3] Martinos Center for Biomedical Imaging, Charlestown, MA, USA

E-mail: spmn@nmr.mgh.harvard.edu and hjcho@unist.ac.kr

Received 8 May 2014, revised 16 August 2014
Accepted for publication 29 August 2014
Published 13 October 2014

**Abstract**

Exploiting the field response of magnetic tracers, magnetic particle imaging (MPI) allows direct, local quantification of the tracer concentration in bulk structures. Here, we investigated the use of characteristic field response functions to spatially resolve the absolute concentration of multiple nanoparticle species by simulation. In particular, using various drive and selection field strengths, we devised color MPI (i.e. cMPI) to quantify and disentangle MPI signals from the mixed Langevin particles of variable concentration and magnetic susceptibility. Specifically, the drive field strength was optimized to distinguish individual field responses from differently sized iron-oxide nanoparticles without compromising the image quality. The proposed cMPI technique is implementable on an existing MPI setup and can be used to quantify biophysical parameters including size-dependent bio-distribution and altered magnetic property of particles. The current study result, simultaneous visualization of the multiple magnetic tracers, theoretically validates the potential feasibility of cMPI as a versatile biosensor and contrast imaging method.

Keywords: magnetic particle imaging, super-paramagnetic iron oxide nanoparticle, contrast agent imaging

(Some figures may appear in colour only in the online journal)

## 1. Introduction

Probe property of magnetic nanoparticles has been actively explored in biomedical science for excellent magnetic resonance imaging (MRI) sensitivity and application-specific

[4] Author to whom any correspondence should be addressed
Unist-gil 50 (100 Banyeon-ri), Eonyang-eup, Uljugun, Ulsan Metropolitan City, Korea 689–798

  

manipulability. Frequently employed as biosensors and imaging contrast medium, such magnetic nanoparticles promoted an array of biomarkers for characterizing biophysical parameters based on magnetic correlates. In particular, super-paramagnetic iron oxide (SPIO) nanoparticles have been often used as blood pool contrast agent and also modified as beacons of specific molecular targets in MRI (Hendrick and Mark Haacke 1993, Thorek *et al* 2006, Andrä *et al* 2007, Pankhurst *et al* 2009, Bulte *et al* 2011). Along with these technical advances and advantages, need for accurate quantification of magnetic particle concentration has become increasingly important.

Although several traditional parameters in MR relaxometry allow quantitative analysis of *in vivo* SPIO concentration in high-resolution MR images, these MR parameters are mostly based on the indirect influence of SPIO particles by the relaxation behavior of nearby protons. Such measures are likely to be affected by factors other than particle concentration, which could result in the diminished accuracy and ambiguity among MRI signal contrasts (Nunn *et al* 1997, Romanusa *et al* 2002). Recently introduced Magnetic Particle Imaging (MPI), first by Gleich *et al* bypasses such limitations and quantifies spatially encoded magnetic signals derived from the magnetic particles, which are precisely proportional to the particle concentration. Strictly based on the magnetic signals derived directly from Langevin particles, the MPI technique holds a great potential for *in vivo* monitoring of tomographic distribution of SPIO particles with high sensitivity, resolution and speed (Gleich and Weizenecker 2005, Gleich *et al* 2008).

With such manifest advantages, MPI has been rapidly gaining attention in the field of biomedical imaging (Weizenecker *et al* 2009, Buzug *et al* 2010). However, despite the related technical improvements, signal source underlying the MPI method has been based solely on the monochromatic modulation of magnetic field. In the current work, dependence of the MPI signal on the characteristic magnetization of nanoparticles was investigated to increase the range and utility of MPI technique. In particular, signal contributions from groups of differently sized SPIO particles were disentangled, in which each characteristic MPI signal was used to quantify the size-dependent particle concentration. Using the conventional MPI reconstruction algorithm based on the field free point (FFP) trajectory (Weizenecker *et al* 2007, Knopp *et al* 2009), we theoretically validated the spatial mapping of both the variable particle size (different magnetization response) and concentration using two (or more) independent measurements at different drive field strengths.

Simultaneous spatial mapping of multiple particle species is potentially important in *in vivo* application of SPIO particles by increasing the number of quantifiable biophysical and magnetic parameters. Resolving the absolute concentrations of biocompatible SPIO particles based on different magnetic properties would provide new biomedical imaging approaches that have not been previously available. In particular, circumventing limitations of MRI and MPI, the proposed color MPI (cMPI) method adds the capability of spectral resolution and improves the current SPIO imaging technique by utilizing the diversity of nonlinear magnetic responses.

## 2. Theory and simulations

The MPI uses the nonlinear response of SPIO nanoparticles in an oscillating magnetic field. The combination of static (selection) and homogeneous oscillating (drive) magnetic fields creates spatial changes of field free point (FFP) over specific region of interest (ROI). Such shifts of FFP enable the spatial encoding of local SPIO distribution, in which an inversion of MPI signal based on the prior knowledge of response function (system function) can be used to produce the spatial mapping of the absolute SPIO concentration (Gleich and Weizenecker 2005, Weizenecker *et al* 2007).

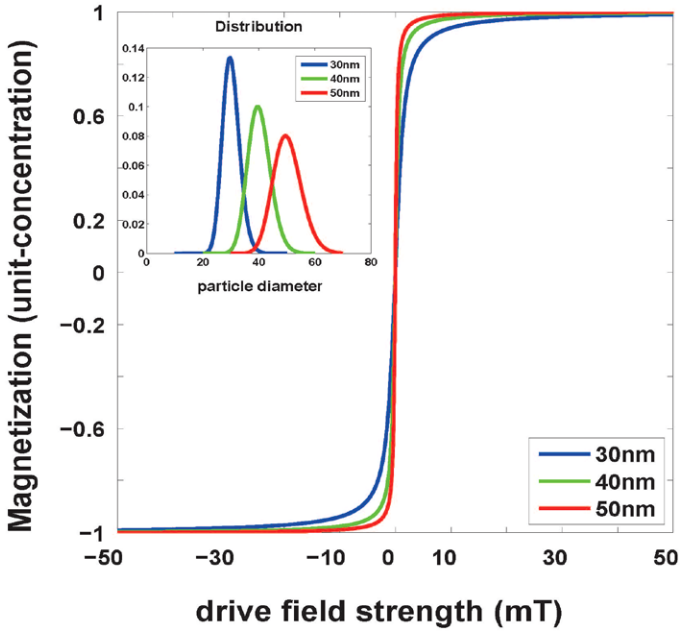


**Figure 1.** Magnetization curves for 30 nm, 40 nm, and 50 nm Langevin particles. Inset figure shows the distribution of each particle used in the calculations.

The magnetization response of SPIO nanoparticles in varying external magnetic field is the key determinant of MPI reconstruction. The dependence between the particle magnetization and external field follows the Langevin function as given by (Hellwege *et al* 1967, Chikazumi and Graham 2009),

$$M(\xi) = M_0(\coth h\xi - 1/\xi) \tag{1}$$

where $M_0$ ($=Nm/\Delta V$) is the saturation magnetization, $N$ is the number of particles in the volume $\Delta V$, and $m$ ($=\pi D^3 M_s/6$) is the magnetic moment related to the particle diameter ($D$). The saturation magnetization ($M_s$) of $Fe_3O_4$ magnetite is $0.6\,\mathrm{T}\mu_0^{-1}$ while $\xi\left(=\mu_0 mH/K_\mathrm{B}T\right)$ is the ratio between magnetic and thermal energies (Hellwege *et al* 1967).

A key property of this relationship is that changes in the diameter of Langevin particles result in different magnetization curves. Such differences in the magnetization profiles for 30 nm, 40 nm, and 50 nm Langevin particles for unit iron concentration are shown in figure 1. The size distribution shown in the inset of figure 1 was used to generate the corresponding magnetization curves for each particle group (Ferguson *et al* 2010),

$$\mathrm{g}(d_0, \sigma, d) = \frac{1}{\sigma d\sqrt{2\pi}} \mathrm{e}^{-\frac{(\ln(d/d_0))^2}{2\sigma^2}} \tag{2}$$

where $d_0$ is mean particle diameter, and $\sigma$ is standard deviation set as 0.1.

When a drive field of $10\,\mathrm{mT}\mu_0^{-1}$ is applied to the particles group, only the magnetization of 50 nm particles is completely saturated as shown in figure 2. Increasing the drive field strength to $20\,\mathrm{mT}\mu_0^{-1}$ induces the magnetizations of smaller particles (i.e. 40 nm particles) to be saturated, but leaves 30 nm particles still responsive to the changes in the external field. Therefore, the distinguishable saturation behavior at different drive filed strength provides the

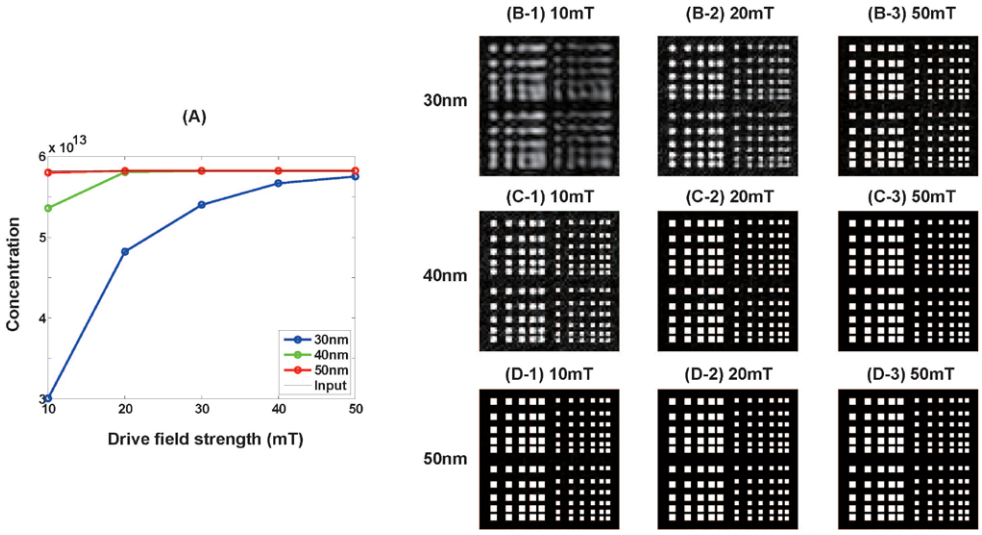


**Figure 2.** (A) Reconstructed signal response of 30 nm, 40 nm, and 50 nm particles as a function of drive field strength. (B-1), (B-2), and (B-3) show reconstructed images of 30 nm particle at 10 mT$\mu_0^{-1}$, 20 mT$\mu_0^{-1}$, and 50 mT$\mu_0^{-1}$, respectively. (C-1), (C-2), and (C-3) show corresponding reconstructed images of 40 nm particle. (D-1), (D-2), and (D-3) show corresponding reconstructed images of 50 nm particle.

key to disentangle different particle groups. Based on these observations, a color MPI (cMPI) experiment is proposed to disentangle signal contributions from the differently sized Langevin particles and to quantify absolute particle concentrations by utilizing multiple MPI signal acquisitions at various drive field strengths. In addition, a strategy for determining weighting factor to measure the compositions of mixed particles was also demonstrated.

### *2.1. Setup and parameters*

The basic simulation scheme and parameters followed the previously reported values used in the MPI acquisition (Weizenecker *et al* 2007). The selection field was applied at a gradient strength of $\partial H_z/\partial z = 2.5\,\mathrm{T}\mu_0^{-1}\,\mathrm{m}^{-1}$, $\partial H_x/\partial x = \partial H_y/\partial y = 1.25\,\mathrm{T}\mu_0^{-1}\,\mathrm{m}^{-1}$ along the $z$-, $x$-, and $y$-direction, respectively. The initial FFP was located at the center of the setup. In order to shift the FFP for spatial encoding, a spatially homogeneous oscillating drive field was applied by varying the amplitude from 10 mT$\mu_0^{-1}$ up to 50 mT$\mu_0^{-1}$ with an interval of 10 mT$\mu_0^{-1}$. The FFP followed the Lissajous trajectory with the specific frequency ratio (i.e. 99/98), in which $f_z = 25.25$ kHz and $f_y = 25.51$ kHz were used. To keep the FOV ($2A/G$, where $A$ is the drive field amplitude and $G$ is the selection field gradient) constant while changing the drive field amplitude, the selection field gradient was adjusted accordingly. The grid size was 64 × 64 with the spatial discretization of 500 $\mu$m × 250 $\mu$m, and the total time required for simulated acquisition was 3.88 ms.

### *2.2. Derivations of induced MPI signal*

The induced MPI signal from the mixture sample model was calculated using the schematic configuration as previously reported (Weizenecker *et al* 2007). Two recording coils have a

quadratic shape with a 10 cm side length. The distance between the recording coil and the center of the FOV (32 mm × 16 mm) was 10 cm apart in both *y*-direction and *z*-direction. The sensitivity of the coil was defined below using the notation previously reported by Weizenecker *et al* (2007),

$$s(\boldsymbol{r}) \equiv \frac{H(\boldsymbol{r}, t)}{i(t)} \equiv \frac{1}{4\pi}\int_{\partial S} \frac{\mathrm{d}\boldsymbol{l} \times (\boldsymbol{r} - \boldsymbol{l})}{\|\boldsymbol{r} - \boldsymbol{l}\|^3} \tag{3}$$

where $\boldsymbol{H}(\boldsymbol{r},t)$ is the strength of applied magnetic field, $i(t)$ is the current, $\partial$S is the boundary of S (surface), $\boldsymbol{r}$ is the location of the particle, and $\boldsymbol{l}$ is the position of the recording coil.

To reduce the burden of computation time, the induced voltage $u(t)$ was expressed using the sensitivity of the coils using equation (2). Then, the signal was calculated using the following equation (Weizenecker *et al* 2007),

$$u(t) = \int_{\mathrm{FOV}} -\mu_0 \frac{\mathrm{d}}{\mathrm{d}t} M(r, t) \cdot s(r) \mathrm{d}r. \tag{4}$$

### 2.3. Calculations of system functions

The system function can be seen as a map describing the spatial sensitivity profile of frequency component. In this study, theoretical calculation of 2D system function was performed as follows. First, a time domain MPI signal by a point-like sample was determined from following equations,

$$S_y(r,t) = -\mu_0 \frac{\mathrm{d}}{\mathrm{d}t} M_y(H(r,t)) \cdot \mathrm{s}(r) \tag{5}$$

$$S_z(r,t) = -\mu_0 \frac{\mathrm{d}}{\mathrm{d}t} M_z(H(r,t)) \cdot \mathrm{s}(r) \tag{6}$$

where,

$$\frac{\mathrm{d}}{\mathrm{d}t} M_y(H(r,t)) = \left( \frac{\partial M_y}{\partial H_y} \cdot \frac{\mathrm{d}H_y}{\mathrm{d}t} + \frac{\partial M_y}{\partial H_z} \cdot \frac{\mathrm{d}H_z}{\mathrm{d}t} \right) \tag{7}$$

$$\frac{\mathrm{d}}{\mathrm{d}t} M_z(H(r,t)) = \left( \frac{\partial M_z}{\partial H_y} \cdot \frac{\mathrm{d}H_y}{\mathrm{d}t} + \frac{\partial M_z}{\partial H_z} \cdot \frac{\mathrm{d}H_z}{\mathrm{d}t} \right) \tag{8}$$

$$H(r,t) = H_s(r) - H_D(t) = \begin{pmatrix} Gx \\ Gy \\ Gz \end{pmatrix} - \begin{pmatrix} 0 \\ A_y \cos w_y t \\ A_z \cos w_z t \end{pmatrix}. \tag{9}$$

Langevin function with particle distribution was used to reflect the realistic magnetization ($\boldsymbol{M}$). The combination of selection field ($\boldsymbol{H}_s$) and drive field ($\boldsymbol{H}_D$) is denoted as $\boldsymbol{H}$. $\boldsymbol{G}$, $\boldsymbol{A}$, and $\boldsymbol{w}$ are the strengths of the selection field gradient, drive field, and the angular frequency of drive fields, respectively. $s(\boldsymbol{r})$ is the sensitivity of coil defined from equation (3).

Then the discretized system functions ($S_n^y$ and $S_n^z$) for both receiver coils were then derived from respective time domain signals of $S_y(r,t)$ and $S_z(r,t)$ by discrete Fourier transformation along the temporal dimension.

### *2.4. The noise addition*

The noise voltage was added to the calculated MPI signal before the image reconstructions using Gaussian random distribution. The noise voltage was obtained using the following scheme (Weizenecker *et al* 2007),

$$U^2_{\text{Noise}} = 4k_{\text{B}}T\Delta f R \tag{10}$$

where $k_{\text{B}}$ is the Boltzmann constant, $T$ is the absolute temperature of 310 K, $\Delta f$ is the bandwidth 1 MHz derived from the sampling time $\Delta t = 1\,\mu$s, and $R$ is the measured resistance of 100 m$\Omega$ (Weizenecker *et al* 2007).

### *2.5. Reconstructions and classifications*

In this study, due to the use of differently sized magnetic nanoparticles, the system functions for both 40 nm and 50 nm particle were separately used for the calculation of induced MPI signal and corresponding reconstructions. Fourier components of MPI signal of the sample for $y$ and $z$ receiver coils were calculated as,

$$U^y_n = \sum_k S^{y1}_{nk} C^1_k + \sum_{k'} S^{y2}_{nk'} C^2_{k'} \tag{11}$$

$$U^z_n = \sum_k S^{z1}_{nk} C^1_k + \sum_{k'} S^{z2}_{nk'} C^2_{k'} \tag{12}$$

where $S^{y1}$, $S^{y2}$, $S^{z1}$, $S^{z2}$ represent discretized system function matrix for $y$- and $z$-receiver coils. $C^1$, $C^2$ denote spatial concentration distribution vectors. Upper scripts 1 and 2 label the 40 nm (1) and 50 nm (2) particle groups, respectively. $k$ and $k'$ are position indexes. $n$ denotes the frequency component, whose cutoff frequency was determined by thresholding with respect to the noise level which was calculated by averaging high harmonics components (~$30 \times f_0$). The number of harmonics was up to 20, including base frequency. Inversion was performed using a zero-order regularization scheme and singular value decomposition (SVD) as previously described by Weizenecker *et al* (Press *et al* 2002, Weizenecker *et al* 2007)

## 3. Methods

For the conceptual validation, MPI reconstruction of a multi-particle model composed of particle groups with diameters of 40 nm and 50 nm was performed. The FOV was set at 32 mm (horizontal) × 16 mm (vertical) with grid size = 64 × 64 with the spatial pixel discretization = 500 $\mu$m × 250 $\mu$m. Using this experimental setup, three aspects of quantitative cMPI of (i) accuracy in absolute concentration of particle groups, (ii) image resolution, and (iii) ability to effectively distinguish mixed particle groups, were investigated.

### *3.1. Distinction of different particle groups and concentration: algorithmic procedure of cMPI*

The process flowchart shown in figure 3 summarizes each procedure of color MPI simulation. First, the system functions corresponding to the 40 nm (S40) and 50 nm (S50) particle groups were calculated using equations (5) and (6), and induced voltage ($U$) from a multi-particle model was generated using equations (11) and (12) with added noise. Reconstructed four

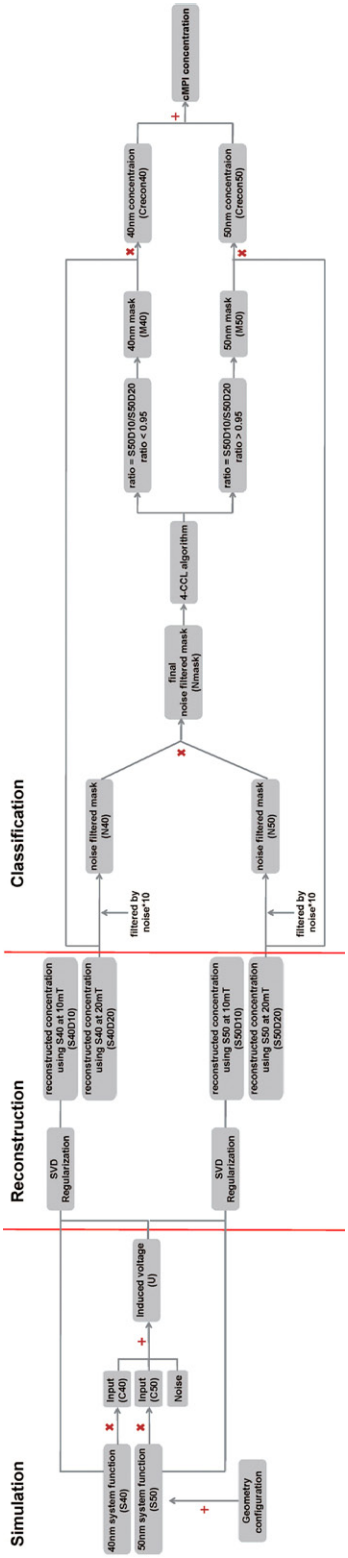


**Figure 3.** Process flowchart for simulation, reconstruction, and classification of cMPI algorithm.

concentration images (S40D10, S40D20, S50D10, and S50D20) were then obtained by applying inversion using either the 40- or 50 nm system function via SVD regularization at drive field strength of $10\,\mathrm{mT}\,\mu_0^{-1}$ and $20\,\mathrm{mT}\,\mu_0^{-1}$, respectively. Second, the noise filtered masks (N40 and N50) were generated by thresholding above 10 times noise level to reduce the distinction error and apply 4-connected-component labeling (4-CCL) method (Rosenfeld and Kak 1976). Final noise filtered mask (Nmask) was generated by taking common intersection of both masks of N40 and N50. Third, 4-CCL algorithm was employed to increase the detection accuracy by filtering any erroneous spatial noises (Rosenfeld and Kak 1976). Finally, the dependence of reconstructed signal on the drive field strength was investigated to determine the difference in the signal responses between the 40 nm and 50 nm particle groups. To exploit the difference between particle groups, the ratio was calculated by dividing the concentration image with S50 inversion at the drive field strength of $10\,\mathrm{mT}\,\mu_0^{-1}$ (S50D10) by that at the drive field strength of $20\,\mathrm{mT}\,\mu_0^{-1}$ (S50D20). Specifically, the cutoff value of the ratio was set at 0.95 because the concentration of 50 nm particle group at drive field strength of $10\,\mathrm{mT}\,\mu_0^{-1}$ is almost same as that at $20\,\mathrm{mT}\,\mu_0^{-1}$, but the concentration of 40 nm particle group is increasing as drive field strength is increasing, which is further explained in the Results section with figure 4. And the ratio of 0.95 was chosen also to eliminate any influence from signal fluctuations up to 5%. Consequently, the concentration ratio above and below 0.95 was identified as the 50 nm and 40 nm particle group, respectively and corresponding masks (M50 and M40) were generated Finally, after distinguishing each particle group, the absolute concentration images (Crecon50 and Crecon40) were generated by combining M50 with S50D20 and M40 with S40D20, respectively. Color MPI image was then obtained by summing Crecon50 and Crecon40.

### *3.2. Quantification of the absolute concentration*

To assess the efficiency of the processing strategy of cMPI, a hypothetical phantom composed of 40 nm and 50 nm particle groups was prepared with varying concentrations from 1*C* to 5*C* (figure 5(A)). The distinction criteria described in the previous flowchart of figure 3 were then sequentially followed and presented with consistent labeling scheme for the categorization of particle size and for the estimation of absolute concentration.

### *3.3. Resolution of cMPI*

To identify the resolution of cMPI, the model was generated as also shown in figure 4(A). In this model, the distances between square regions were varied from one to five pixels for assessing image resolution limit. And the number of voxels for square was set to four and nine to validate feasible minimum number of voxels for 4-CCL method because 4-CCL counts the connected voxel as the same particle group. For example, achievable spatial resolution using 4-CCL method is $1000\,\mu$m (horizontal) $\times$ $500\,\mu$m (vertical) if the square containing four voxels is distinguishable. Furthermore, this process was also repeated for multiple concentrations (774, 77.4, and $7.74\,\mu$mol (Fe) $l^{-1}$) to verify the imaging resolution limit as a function of the iron concentration.

### *3.4. Determination of weighting factor for mixed particles*

The feasibility of distinguishing differently weighted mixtures of 40 nm and 50 nm particle groups was also investigated. Five different mixtures with weightings of [0, 1], [0.2, 0.8], [0.5, 0.5], [0.8, 0.2], and [1, 0] were prepared, where the values in brackets represent the relative

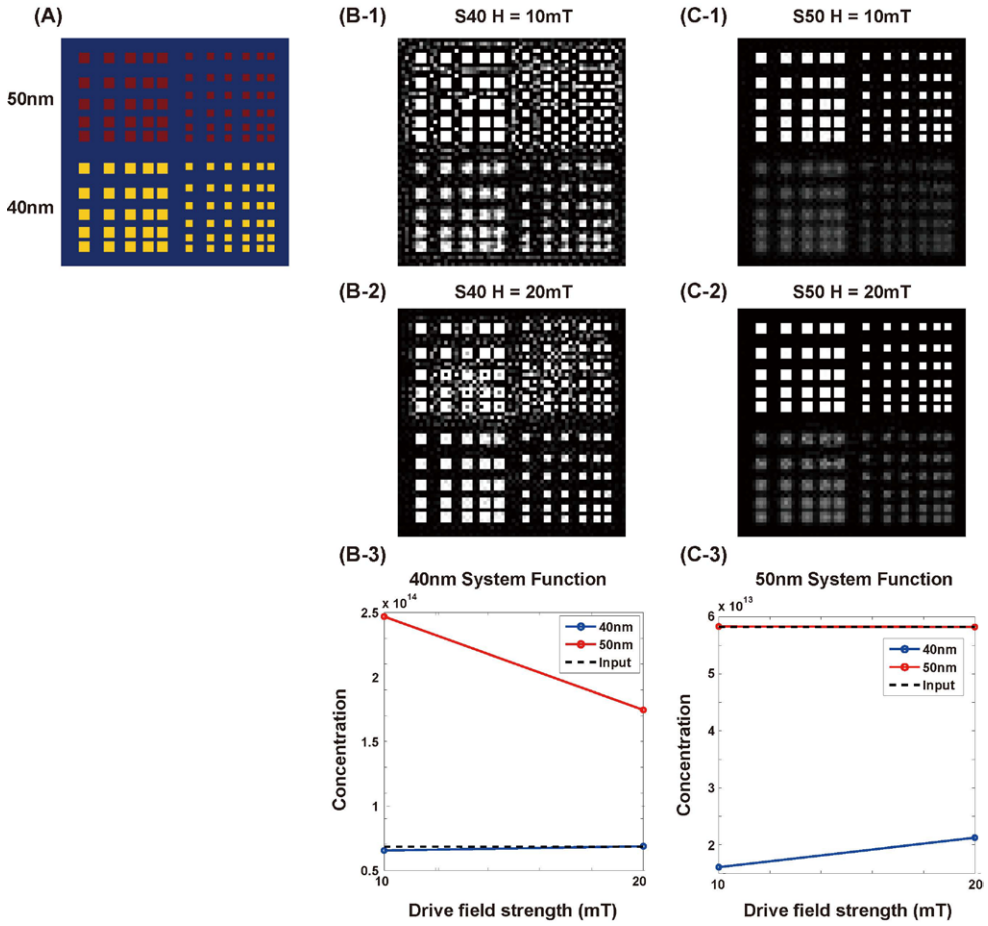


**Figure 4.** (A) Representative sample model with differently-sized particle groups with diameters of 40 nm (bottom) and 50 nm (top). (B-1) and (B-2) show reconstructed images with 40 nm system function at 10 mT $\mu_0^{-1}$ and 20 mT $\mu_0^{-1}$, respectively. (C-1) and (C-2) show reconstructed images with 50 nm system function at 10 mT $\mu_0^{-1}$ and 20 mT $\mu_0^{-1}$, respectively. (B-3) plots the representative signal response of 40 nm and 50 nm particle groups as a function of drive field strength when reconstructed with 40 nm system function (S40). (C-3) plots corresponding signal response with 50 nm system function (S50).

weightings of the 40 nm and 50 nm particle groups, respectively. First, the concentration measurement of particle mixtures to varying drive field was reconstructed using the 50 nm system function. These signals were then normalized by the concentration calculated at the drive field strength of 10 mT $\mu_0^{-1}$. In particular, the dependence of this normalized concentration on variable drive field strengths was investigated to establish an monotonic, linear relationship between the mean concentration ratio (i.e. C(20 mT $\mu_0^{-1}$) / C(10 mT $\mu_0^{-1}$)) and particle weighting. Based on these results, the mean concentration ratio of each particle mixture was fitted as the weighted sum of single particle group values (e.g. a combination of 40- and 50 nm), which revealed the respective weighting of each particle group. Thereafter, to further improve the quantification accuracy, system function for the average particle size of each mixture was selected based on the estimated weighting factor and used for the determination of total particle concentration.

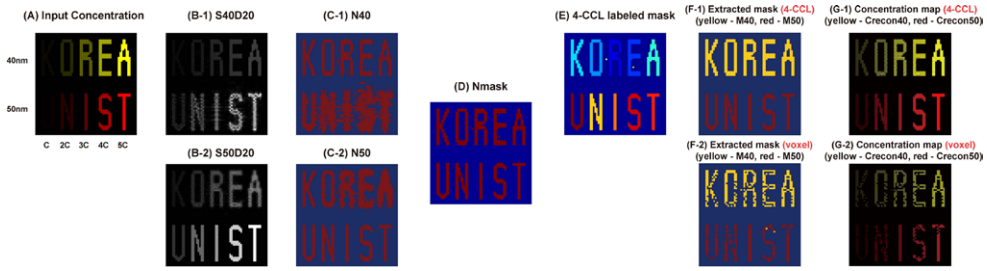


**Figure 5.** (A) Representative sample model with differently-sized particle groups between the rows and increasing concentration across the columns. (B-1) Reconstructed concentration map using S40 at drive field strength of $20\,\mathrm{mT}\,\mu_0^{-1}$. (B-2) Reconstructed concentration map using S50 at drive field strength of $20\,\mathrm{mT}\,\mu_0^{-1}$. (C-1) Noise filtered mask from (B-1). (C-2) Noise filtered mask from (B-2). (D) Final noise filtered mask multiplying (C-1) with (C-2). (E) 4-CCL labeled mask. (F-1) Extracted mask using distinction criteria with 4-CCL approach. (F-2) Extracted mask using distinction criteria with voxel-wise approach. (G-1) cMPI concentration map with 4-CCL approach. (G-2) cMPI concentration map with voxel-wise approach.

## 4. Results

### *4.1. Distinction of different particle groups and quantification of the absolute concentration*

Reconstructed images of the multi-particle model (figure 4(A)) using the single system function S40 (i.e. that for 40 nm particle group) for drive field strengths of $10\,\mathrm{mT}\,\mu_0^{-1}$ and $20\,\mathrm{mT}\,\mu_0^{-1}$ are shown in figures 4(B-1) and (B-2), respectively. Similarly, figures 4(C-1) and (C-2) show those reconstructed using the system function S50 (i.e. that for 50 nm particle group). The dependence of concentration on the drive field strength (between $10\,\mathrm{mT}\,\mu_0^{-1}$ and $20\,\mathrm{mT}\,\mu_0^{-1}$) is shown in figure 4(B-3) for both 40 nm and 50 nm particle groups, which was reconstructed using S40. The reconstruction using S40 results in an overestimation of the 50 nm particle group concentration, which decreased as the drive field increases from $10\,\mathrm{mT}\,\mu_0^{-1}$ to $20\,\mathrm{mT}\,\mu_0^{-1}$. In contrast, the reconstructed 40 nm particle group concentration using S40 accurately estimated the input concentration at drive field strength of $20\,\mathrm{mT}\,\mu_0^{-1}$. Similarly, figure 4(C-3) demonstrates the concentration of both 40 nm and 50 nm particle groups reconstructed using S50. In this case, the reconstruction using S50 significantly underestimated the 40 nm particle group concentration, which increased with the increasing drive field. The 50 nm particle group concentration reconstructed using S50 also matched the input concentration at both drive field strengths. Based on the characteristic behavior of each particle type at different drive field strengths, the distinction criteria were developed to produce a corresponding particle-size mask.

To demonstrate the quantification efficiency and this distinction criteria consistent with the steps presented in the flowchart of figure 3, an alphabetical model was created (see figure 5(A)). First, thresholding of noise was performed on the reconstructed concentration using S40 at drive field strength of $20\,\mathrm{mT}\,\mu_0^{-1}$ (S40D20—figure 5(B-1)) to obtain noise filtered mask for 40 nm particle group (N40—figure 5(C-1)). Thresholding value was determined by acquiring the average signal value of the noise region and multiplying by a factor of 10. In the same way, the noise filtered mask for 50 nm particle group (N50—figure 5(C-2)) was also extracted using the reconstructed concentration using S50 at drive field strength of $20\,\mathrm{mT}\,\mu_0^{-1}$ (S50D20—figure 5(B-2)). In N40, the noise thresholding worked well in 40 nm particle group region, but 50 nm particle group region was blurred as shown in figure 5(C-1). On the other

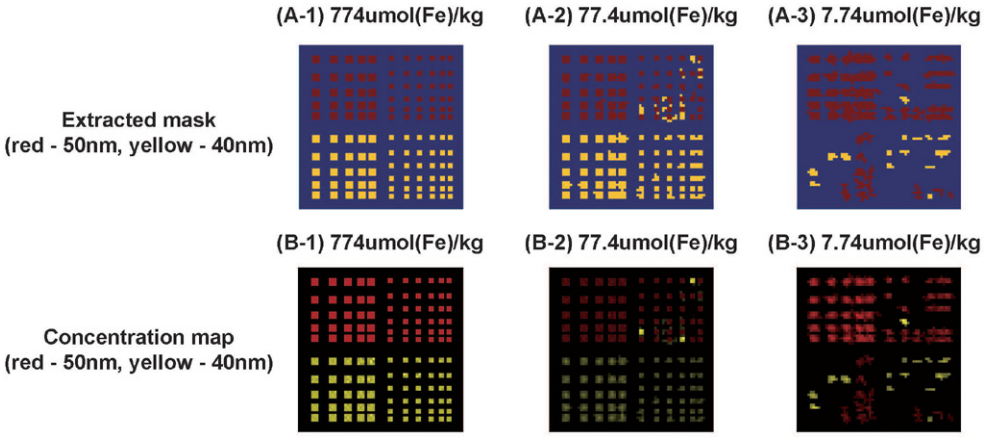


**Figure 6.** (A-1), (A-2), and (A-3) show particle size resolved mask of sample model at different unit concentration of 774 $\mu$mol (Fe) $l^{-1}$, 77.4 $\mu$mol (Fe) $l^{-1}$, and 7.74 $\mu$mol (Fe) $l^{-1}$, respectively. (B-1), (B-2), and (B-3) show corresponding cMPI reconstructions. The concentration of each particle type was determined from the reconstruction at 20 mT $\mu_0^{-1}$ with the respective system functions.

hand, the noise extracting was clear in 50 nm particle group region, but blurred in 40 nm particle group in N50. To acquire combined noise filtered mask, N40 and N50 were multiplied to extract the common intersection of the two masks and depicted as final noise filtered mask (Nmask) as shown in figure 5(D). Second, the 4-CCL method was used to construct labeled masks using Nmask as shown in figure 5(E). For example, alphabet K in figure 5(E) has single colored mask which means this mask region is composed of same particle group. Therefore, the concentration is averaged using the mask, which increased the accuracy in distinction due to the higher sensitivity than voxel-wise processing. Third, the ratio between the concentration measurements using the drive field strengths of 10 mT $\mu_0^{-1}$ and 20 mT $\mu_0^{-1}$ was calculated to classify the particle type in the 4-CCL mask and the cutoff value of this concentration ratio was set at 0.95 as explained in Method section. The concentration ratio (S50D10/S50D20) below 0.95 was identified as the 40 nm particle group (M40) and above 0.95 was defined as the 50 nm particle group (M50). Such classification strategy resulted in two particle masks, as shown in figure 5(F-1).

As the matching system function accurately reproduced the absolute concentration of each particle type (see in figures 4(B-3) and (C-3)), the concentration image was obtained using the system functions specific for the assigned particle size at a drive field strength of 20 mT $\mu_0^{-1}$. With the application of acquired masks, the final cMPI image was constructed (red: 50 nm; yellow: 40 nm) as shown in figure 5(G-1), which faithfully reproduced the original input model. Additionally, the voxel-wise approach was performed with the same distinction criteria. The extracted mask was shown in figure 5(F-2) and the corresponding final cMPI image was shown in figure 5(G-2). Compared to 4-CCL method, voxel-wise method causes more error.

### *4.2. Resolution of cMPI*

To identify the resolution of cMPI, the model with iron concentration of 774 $\mu$mol (Fe) $l^{-1}$ was generated and distinction criteria was performed as shown in figures 6(A-1) and (B-1). The

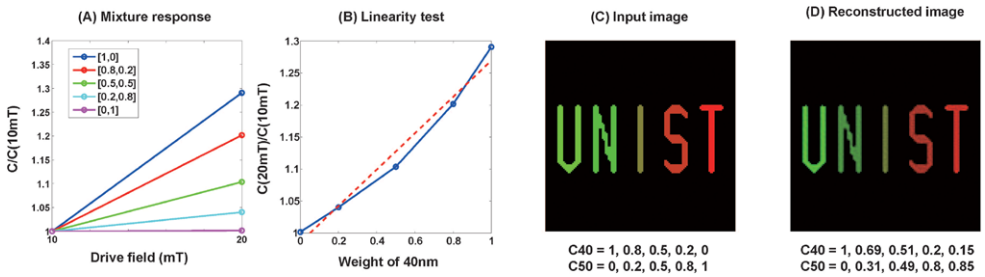


**Figure 7.** (A) The drive field-dependent responses of five mixtures with different weightings of 40 nm and 50 nm obtained using 50 nm system function for reconstruction. Five different mixtures with weightings of [1, 0], [0.8, 0.2], [0.5, 0.5], [0.2, 0.8], and [0, 1] were prepared, where the values in the brackets represent the relative weightings of the 40- and 50 nm particles, respectively. (B) Linearity test between the weighting of 40 nm particle and the drive field-dependent responses. Solid line is acquired points and dashed line is linear fitted curve. Comparison between input (C) and reconstructed images (D) for mixtures with different concentration weighting of 40 nm and 50 nm particles. Green and red colors are assigned for [1,0] and [0,1] mixture, respectively.

extracted mask showed that every square is distinguishable, which results in the achievable spatial resolution of 500 $\mu$m. Moreover, cMPI images were also obtained for reduced iron concentrations of 77.4 $\mu$mol (Fe) $l^{-1}$ (figures 6(A-2) and (B-2)) and 7.74 $\mu$mol (Fe) $l^{-1}$ (figures 6(A-3) and (B-3)). As the iron concentration decreased, decreases in the signal strength led to the concomitant deterioration in the de finition of particle-size masks and corresponding absolute iron concentration. As shown in figure 6(A-2), the closest particle groups (one voxel distance) were starting to get connected to each other, which means that these groups were not distinguishable using 4-CCL method anymore. For this reason, the achievable spatial resolution is reduced to about 1 mm at iron concentration of 77.4 $\mu$mol (Fe) $l^{-1}$. In the case of 7.74 $\mu$mol (Fe) $l^{-1}$, the signals from 40 nm particle group region were not visible due to lowered sensitivity with respect to that from 50 nm particle group. And the achievable spatial resolution of 50 nm particle group was further reduced to about 2 mm.

### *4.3. Determination of weighting factor for mixed particles*

Finally, five mixtures with different unit-normalized particle weightings ([0, 1], [0.2, 0.8], [0.5, 0.5], [0.8, 0.2], and [1, 0]) were examined to verify the feasibility of quantifying the composition of 40 nm and 50 nm particle groups within an image voxel. As shown in figure 7(A), each mixture showed different dependences (i.e. slopes) on the drive field strength (between 10 mT $\mu_0^{-1}$ or 20 mT $\mu_0^{-1}$) for the S50 system function reconstruction. In general, the reconstructed signals increased with the increasing drive field strength and were dependent on the composition of differently weighted mixture. Note the drive field independence of 50 nm particle group (i.e. flat) with the use of matching system function as explained above. The slope between the normalized signal strength ratio and drive field was the lowest at [0, 1] while the increase in 40 nm particle group weighting monotonically elevated the slope, which reached the maximum at [1, 0]. This linearly increasing signal dependence (i.e. slope) shown in figure 7(B) suggests that the signal strength of each mixture may be approximated by a linear superposition of the drive field dependence of the [1, 0] and [0, 1] mixtures, i.e. $\text{Slope}_{[a,\,b]} = a \times \text{Slope}_{[1,\,0]} + b \times \text{Slope}_{[0,\,1]}$. Constants, $a$ and $b$ represent the respective

weightings of the 40 nm and 50 nm particle groups, and $\text{Slope}_{[a,\,b]}$, $\text{Slope}_{[1,\,0]}$, and $\text{Slope}_{[0,\,1]}$ represent the slopes of the signal strength between the two drive field strengths of $10\,\text{mT}\,\mu_0^{-1}$ and $20\,\text{mT}\,\mu_0^{-1}$ for the mixtures of [$a$, $b$], [1, 0], and [0, 1], respectively.

Figure 7(C) shows the input image of five different mixtures as described above, where green and red represent the 40 nm and 50 nm particle groups, respectively. On this sample image, the values of $a$ and $b$ were fitted using the proposed linear estimation method to determine the weighting of each particle group as shown in the lower caption of figure 7(D). The deviation of each estimated weighting from the true value is likely due to the imperfect linearity of intensity slope versus 40 nm weightings as shown in figure 7(B). In addition, to accurately measure the absolute concentration, the optimal system functions were selected for each mixture, which were applied to calculate the total particle concentration. For example, in the case of a particle mixture [0.8, 0.2], the estimated weighting was [0.69, 0.31]. By choosing an integer closest to the average particle size, the 43 nm system function was applied to quantify the absolute concentration. Following this quantification strategy, the reconstructed cMPI image of mixed particles was obtained as shown in figure 7(D), which reveals a close semblance to the original input image.

## 5. Discussion

Further implementing on the MPI, here we investigated and exploited the divergent signal dependence on the drive field strength to distinguish different Langevin particle species without sacrificing measurement accuracy. Based on the reconstructed signal change as a function of drive field strength, the distinction criterion was determined to disentangle MPI signals from multiple particle groups. The reconstructed dependence curve using S50, the magnetic signals from the 50 nm particle groups were completely saturated beyond the drive field strength of $10\,\text{mT}\,\mu_0^{-1}$. In contrast, as revealed in the corresponding signal dependence curve (figure 4(C-3)), the 40 nm- particle showed a significant signal difference between the drive fields at $10\,\text{mT}\,\mu_0^{-1}$ and $20\,\text{mT}\,\mu_0^{-1}$. Such signal mismatch between the system functions and particle sizes provided the rationale for determining the distinction criterion, which was applied to map the concentration of two differently sized particle groups. In particular, a reconstructed signal ratio of 0.95 between two drive fields was used as the cutoff threshold to divide drive field-dependent saturation profiles. It is notable that for distinguishing additional and/or other particle groups with different magnetic property, such deterministic criteria should be reevaluated prior to each study.

Furthermore, a feasibility test for the quantification of mixed particles was performed. For the spatially co-localized particles, the normalized concentration of the particle mixture was strongly dependent on the drive field strength as well as the particle weighting (i.e. variable slopes in figure 7(A)). Interestingly, changes in this dependence (slope) were almost linearly proportional to the particle weighting as shown in figure 7(B), which enabled the estimation of particle weighting via simple linear superposition. This particular feature of cMPI will be highly useful for the simultaneous determination of different particle weighting factors within a voxel. However, apparent error in the weighting estimation shows the presence of inherent methodological error due to the imperfect linearity shown in figure 7(B). Such measurement error warrants thorough characterization and optimization of the technique.

As for biomedical application, SPIO-based tracking of therapeutic or stem cells *in vivo* can be aided by the cMPI method to determine its delivery efficacy in a multi-faceted manner before directly assessing the function of target organs. In addition to the quantitative feedback of highly

sensitive MPI, the proposed cMPI will provide an opportunity for simultaneously tracking cells loaded with different SPIO particles. The spatial registration of multiple cell types with variable magnetic activities may optimize and diversify the treatment processes for a variety of neural and degenerative diseases such as stroke (Savitz *et al* 2004, Shyu *et al* 2006, Chang *et al* 2007), Parkinson's (Lindvall 2003, Lindvall and Björklund 2004, Lindvall and Kokaia 2009), diabetes and Alzheimer's diseases (Mattson 2000, Soria *et al* 2001, Hussain and Theise 2004, Kim and De Vellis 2009). Moreover, the added advantage of size-dependent signal separation could easily lead to the direct quantification of the distribution characteristics of differently sized SPIO species. Specifically, each tissue compartment, only accessible to particular SPIO can be independently calculated, thus bypassing other model-based imaging approaches (Kim *et al* 2002, 2004). On the other hand, the magnetic selectivity of cMPI technique may offer a new means and devices to measure the exact diameter, magnetic property and composition of the synthesized particles.

Even though the current study is a theoretical verification, the use of already proven conventional MPI reconstruction algorithms free of significant modifications on the existing hardware may allow facile implementation of the cMPI method. However, a few technical limitations of cMPI are worth noting. First, the doubled temporal resolution will be inevitable due to the requirement of at least two MPI acquisitions for cMPI using multiple drive fields. For this reason, dynamic study using cMPI at high temporal resolution would be more challenging than conventional MPI, which typically operates at ~40 msec/image. Secondly, unless exact types of particles are known *a priori*, classifying particle species would be difficult for cases of particles with different magnetism coexisting in the same voxel. Future works should therefore include developing more efficient method to extract the particle weighting factor for quantifying spatially mixed particles. The possible range of dynamic field strength and particle size may be limited for the immediate biomedical applications. In this work, we fixed the maximum drive field strength to be $20\,\mathrm{mT}\,\mu_0^{-1}$ at the selection field strength of $2.5\,\mathrm{T}\,\mu_0^{-1}\,\mathrm{m}^{-1}$ with iron concentration of $774\,\mu$mol (Fe) $l^{-1}$, which made us choose 40 nm, 50 nm particle to obtain reasonable image quality as also can be seen from the previous work. (Weizenecker *et al* 2007). Possible approaches to make this work more *in vivo* compatible are two folds. First, as the size is not necessarily the only parameter that changes magnetization behavior of nanoparticles, different strategy, such as doping may be employed to alter the magnetization behavior of nanoparticles to alleviate the particle size restrictions for realistic applications. At the same time, acquisition parameters which less affect *in vivo* applications, such as the strength of selection field, acquisition times, or noise level may be further optimized in the future experimental work to alleviate any physiologically adverse *in vivo* effects, or available particle sizes.

Monitoring the spatial and dynamic distributions of exogenous SPIO nanoparticles and concentration has been important and also challenging, especially for *in vivo* studies where heterogeneous tissue structure often interferes with the measurement accuracy. In additional support of MPI, the currently proposed cMPI method is designed to resolve the absolute concentration of multiple SPIO nanoparticle species, which will be useful in various biomedical applications where the tracking and quantification of multiple magnetic tracers are beneficial.

## Acknowledgements

This work was supported by the National Research Foundation of Korea Grants funded by the Korean Government (No. 2010-0028684 and No. 2014008255).

## References


Andrä W, Häfeli U, Hergt R and Misri R 2007 Application of magnetic particles in medicine and biology *Handbook of Magnetism and Advanced Magnetic Materials* ed H Kronmüller and S Parkin (Chichester: Wiley) vol. 4

Bulte J W M, Walczak P, Gleich B, Weizenecker J, Markov D E, Aerts H C, Boeve H, Borgert J and Kuhn M 2011 MPI cell tracking: what can we learn from MRI? *Proc. Soc. Photo. Opt. Instrum. Eng.* **7965** 79650z

Buzug T M, Borgert J, Knopp T, Biederer S, Sattel T F, Erbe M and Lüdtke-Buzug K 2010 *Magnetic Nanoparticles: Particle Science, Imaging Technology, and Clinical Applications Proc. of the First Int. Workshop on Magnetic Particle Imaging* (Institute of Medical Engineering, University of Lubeck, Germany) (World Scientific Publishing and Imperial College Press)

Chang Y C, Shyu W C, Lin S Z and Li H 2007 Regenerative therapy for stroke *Cell. Transplant.* **16** 171–81

Chikazumi S and Graham C D 2009 *Physics of Ferromagnetism* vol **94** (Oxford: Oxford University Press)

Ferguson R M, Khandhar A P, Minard K R and Krishnan K M 2010 Size-optimized magnetite nanoparticles for magnetic particle imaging *Magnetic Nanoparticles: Particle Science, Imaging Technology, and Clinical Application* (University of Washington: World Scientific Publishing Co) pp 53–9

Gleich B and Weizenecker J 2005 Tomographic imaging using the nonlinear response of magnetic particles *Nature* **435** 1214–7

Gleich B, Weizenecker J and Borgert J 2008 Experimental results on fast 2D-encoded magnetic particle imaging *Phys. Med. Biol.* **53** N81

Hellwege K H and Green L C 1967 Landolt–Börnstein numerical data and functional relationships in science and technology *Am. J. Phys.* **35** 291–2

Hendrick R E and Mark Haacke E 1993 Basic physics of MR contrast agents and maximization of image contrast *JMRI-J. Magn. Reson. Imaging* **3** 137–48

Hussain M A and Theise N D 2004 Stem-cell therapy for diabetes mellitus *Lancet* **364** 203–5

Kim S U and De Vellis J 2009 Stem cell-based cell therapy in neurological diseases: a review *J. Neurosci. Res.* **87** 2183–200

Kim Y, Rebro K and Schmainda K 2002 Water exchange and inflow affect the accuracy of T1-GRE blood volume measurements: Implications for the evaluation of tumor angiogenesis *Magn. Reson. Med.* **47** 1110–20

Kim Y, Savellano M, Savellano D, Weissleder R and Bogdanov A 2004 Measurement of tumor interstitial volume fraction: method and implication for drug delivery *Magn. Reson. Med.* **52** 485–94

Knopp T, Biederer S, Sattel T, Weizenecker J, Gleich B, Borgert J and Buzug T M 2009 Trajectory analysis for magnetic particle imaging *Phys. Med. Biol.* **54** 385

Lindvall O 2003 Stem cells for cell therapy in Parkinson's disease *Pharmacol. Res.* **47** 279–87

Lindvall O and Björklund A 2004 Cell therapy in Parkinson's disease *NeuroRx* **1** 382–93

Lindvall O and Kokaia Z 2009 Prospects of stem cell therapy for replacing dopamine neurons in Parkinson's disease *Trends. Pharmacol. Sci.* **30** 260–67

Mattson M 2000 Emerging neuroprotective strategies for Alzheimer's disease: dietary restriction, telomerase activation, and stem cell therapy *Exp. Gerontol.* **35** 489–502

Nunn A, Linder K and Tweedle M 1997 Can receptors be imaged with MRI agents? *Q. J. Nucl. Med.* **41** 155–62

Pankhurst Q, Thanh N, Jones S and Dobson J 2009 Progress in applications of magnetic nanoparticles in biomedicine *J. Phys. D Appl. Phys.* **42** 224001

Press W H, Teukolsky S A, Vetterling W T and Flannery B P 1992 *Numerical Recipes in C: The Art of Scientific Computing* 2nd ed. (Cambridge: Cambridge University Press)

Romanusa E, Hückelc M, Großa C, Prassb S, Weitschiesa W, Bräuerc R and Weberb P 2002 Magnetic nanoparticle relaxation measurement as a novel tool for *in vivo* diagnostics *J. Magn. Magn. Mater.* **252** 387–9

Rosenfeld A and Kak A C 1976 *Digital Picture Processing* (New York: Academic Press)

Savitz S I, Dinsmore J H, Wechsler L R, Rosenbaum D M and Caplan L R 2004 Cell therapy for stroke *NeuroRX* **1** 406–14

Shyu W C, Lee Y J, Liu D D, Lin S Z and Li H 2006 Homing genes, cell therapy and stroke *Front. Biosci.* **11** 899–907

Soria B, Skoudy A and Martin F 2001 From stem cells to beta cells: new strategies in cell therapy of diabetes mellitus *Diabetologia* **44** 407–15

Thorek D L J, Chen A K, Czupryna J and Tsourkas A 2006 Superparamagnetic iron oxide nanoparticle probes for molecular imaging *Ann. Biomed. Eng.* **34** 23–38

Weizenecker J, Borgert J and Gleich B 2007 A simulation study on the resolution and sensitivity of magnetic particle imaging *Phys. Med. Biol.* **52** 6363

Weizenecker J, Gleich B, Rahmer J, Dahnke H and Borgert J 2009 3D real-time *in vivo* magnetic particle imaging *Phys. Med. Biol.* **54** L1